Boundary-Layer Meteorology
https://doi.org/10.1007/s10546-021-00687-1

RESEARCH ARTICLE

The Heat-Flux Imbalance: The Role of Advection and Dispersive Fluxes on Heat Transport Over Thermally Heterogeneous Terrain

Travis Morrison[1] · Eric R. Pardyjak[1] · Matthias Mauder[2] · Marc Calaf[1]

Received: 31 December 2020 / Accepted: 29 December 2021

Abstract
Data from the Idealized Planar-Array experiment for Quantifying Spatial heterogeneity are used to perform a control volume analysis ($400 \times 400 \times 2$ m^3) on the total derivative of the temperature tendency equation. Analysis of the heat-flux imbalance, which is defined as the ratio of the sum of advective, dispersive, and turbulence-flux terms to the turbulence-flux term, are presented. Results are divided amongst free-convective and forced-convective days, as well as high-wind-speed and quiescent nocturnal periods. Findings show that the median flux imbalance is greater on forced-convective days (a 168% turbulence-flux overestimation, or relative importance of the advection to dispersive flux to the turbulence flux) when compared to free-convective periods (79% turbulence-flux overestimation). During nocturnal periods, a median turbulence-flux underestimation of 146% exists for quiescent nights and a 43% underestimation of the flux for high-wind-speed nights. These results support the existing literature, suggesting that mean air-temperature heterogeneities lead to strong bulk advection and dispersive fluxes. A discussion of the impact of the flux imbalance on the surface energy balance and numerical-weather-prediction modelling is presented.

Keywords Idealized Planar-Array experiment for Quantifying Spatial heterogeneity · Surface energy balance · Surface fluxes

1 Introduction

Several hypotheses have been proposed to explain the apparent non-closure of the surface energy balance (SEB) (Culf et al. 2004; Foken 2008; Mauder et al. 2020). Some of these include the use of inappropriate (too short) time averaging (Finnigan et al. 2003), instrumenta-

✉ Travis Morrison
travis.morrison@utah.edu

Marc Calaf
marc.calaf@utah.edu

[1] Department of Mechanical Engineering, University of Utah, Salt Lake City, Utah, USA

[2] Institute of Meteorology and Climate Research - Atmospheric Environmental Research, Karlsruhe Institute of Technology, Garmisch-Partenkirchen, Germany

Published online: 07 February 2022

tion limitations (i.e. transducer shadowing, Horst et al. 2015), underestimation of the ground storage (Peters-Lidard et al. 1998; Kukharets and Tsvang 1999; Kukharets et al. 2000; Culf et al. 2004; Higgins 2012), the effect of spatial variability (De Roo and Mauder 2018), and a lack of consideration of advective fluxes (Paw et al. 2000; Oncley et al. 2007; Garcia-Santos et al. 2019). Numerically, high-resolution simulations without land-surface models approach this topic by generating a new understanding of the transport terms of heat. For example, in the flux-imbalance work of Kanda et al. (2004), idealized and realistic three-dimensional information describing the atmospheric-boundary-layer flow field was generated using large-eddy simulations (LES) (Kanda et al. 2004). From this dataset, the standard covariance terms were computed assuming the existence of a single measuring point in the middle of the domain (as a proxy for a traditional eddy-covariance tower). These terms were then compared to the alternative spatially complete information from the simulations. From these results, the authors derived an imbalance term, which was then hypothesized to explain the non-closure of the SEB. One of the main limitations of their work is that they enforced conservation of mass within their limited domain, which results in a domain-averaged vertical velocity component equal to zero, hence artificially reducing the contribution of the bulk advection terms to the imbalance analysis. Moreover, their work only considered the vertical flux contribution, imposing spatial homogeneity, an assumption which fails under most realistic conditions. This work was later revisited by Zhou et al. (2018a), who performed a similar imbalance analysis over an idealized set of temperature patches using the Weather Research and Forecasting (WRF) model over a diurnal cycle. Results showed that daytime surface heating increased the flux imbalance and confirmed the results from Kanda et al. (2004) that heterogeneous surfaces increase the flux imbalance when compared to the homogenous cases.

In our study we revisit the imbalance analysis of Kanda et al. (2004) without the assumptions on the contribution of horizontal transport terms (i.e., horizontal advection and horizontal flux divergence). To accomplish this, data from the Idealized Planar-Array experiment for Quantifying Spatial (IPAQS) heterogeneity campaign are used to compute the volumetric heat transport at scales of 400 m, expanding upon the analysis of the differential form of the tendency equation at 20-m scales used in Morrison et al. (2020). This control volume analysis provides a framework for understanding the contribution of mean fluxes induced by spatial heterogeneity with the goal of further determining the conditions that lead to mean advective and dispersive fluxes. The relevance of this analysis comes to light when considering the equivalent space–time decomposition approach used in numerical-weather-prediction (NWP) models, which often neglect or model local advective or dispersive contributions to the total flux (Margairaz et al. 2020b).

The paper is organized such that in Sect. 2 we provide a review of the time–space filtering of the temperature tendency equation and present an imbalance analysis based on Kanda et al. (2004). Thereafter, in Sect. 3, we provide an overview of the dataset used and methods applied for post-processing the data. In Sect. 4, we present the contribution of the different terms, whose implications are further discussed in Sect. 5. Finally, the conclusions and final remarks are provided in Sect. 6.

2 Theory

The evolution of temperature T in the atmosphere is a function of time and space, and it is mathematically described by the instantaneous and local enthalpy equation as

$$\frac{DT}{Dt} = Sources + Sinks, \tag{1}$$

where the nature of the *Sources* and *Sinks* may vary depending on local thermal forcings. Hence, the experimental techniques used to provide an accurate measure of these terms should in principle also cover both space and time degrees of freedom. However, in practice, micrometeorological measurements typically rely on the ergodicity assumption, employing tower-based systems that are based on fixed-point, time-varying quantities. Therefore, it is useful to expand the left-hand side (l.h.s) of the enthalpy equation Eq. 1 to better reflect the Eulerian nature of the measurements, thus separating the material derivative into a local time variation term and an advective term,

$$\frac{DT}{Dt} = \frac{\partial T}{\partial t} + \frac{\partial}{\partial x_j}(u_j T), \tag{2}$$

where u_j is the velocity in the directions x_j, and t is time. Further, to better illustrate the nature of the time-varying measurements, it is customary to separate the instantaneous signal into a time-averaged or slow-evolving mean term, indicated here by an overbar, and a fluctuating term or fast-evolving turbulence contribution, indicated here with a single prime. Note here that the equations from this point are expressed in index notation, where the subscript j takes on the values 1, 2, or 3, representing the three Cartesian coordinates. Thus, Reynolds averaging is applied such that,

$$u_j(x_j, t) = \overline{u_j(x_j)} + u_j'(x_j, t), \tag{3}$$

$$T(x_j, t) = \overline{T(x_j)} + T'(x_j, t). \tag{4}$$

Normally, either due to technical limitations, or for simplicity, the mean flow is assumed to be steady, horizontally homogeneous, and absent of local subsidence, hence allowing for single point-based eddy-covariance measurements. This leads to the elimination of the time-varying and bulk-advection terms on the right-hand side (r.h.s.) of Eq. 2, leaving only the fluctuating terms. Nonetheless, if one is to only consider the assumption of a local steady state and keep the divergence term for the sake of completeness or discussion, then the r.h.s. of Eq. 2 can be rewritten as

$$\overline{\frac{\partial}{\partial x_j}\left(u_j T\right)} = \frac{\partial}{\partial x_j}\left[\overline{u}_j \overline{T} + \overline{u_j' T'}\right]. \tag{5}$$

In Eq. 5, the cross terms (products of mean terms and fluctuating terms) have been dropped assuming a clear scale separation between the mean term and the turbulence fluctuation (Mason 1995). To compare results from fixed-point and time-dependent measurements (e.g., eddy-covariance methods) with those of spatial- and time-dependent measurements (e.g., unmanned aerial vehicles, plane-based measurements, etc.) or numerical simulations, it is instructive to consider the integration of a set of point measurements over a controlled region of study, or a control volume (Kanda et al. 2004; Pardyjak et al. 2018; Desai et al. 2018; Margairaz et al. 2020a). In this case, the contribution from the advective term in Eq. 5 can be written as

$$\int_{CV} \frac{\partial}{\partial x_j}\left(\overline{u_j T}\right) dV = \int_{CV} \frac{\partial}{\partial x_j}\left[\overline{u}_j \overline{T} + \overline{u_j' T'}\right] dV. \tag{6}$$

Here the subscript CV has been used to refer to the integral over the control volume V. The mean flux term on the r.h.s. of Eq. 6 may be written as follows using the product rule

$$\int_{CV} \frac{\partial}{\partial x_j}\left(\overline{u_j}\,\overline{T}\right) dV = \int_{CV} \overline{u_j}\frac{\partial \overline{T}}{\partial x_j}\, dV + \int_{CV} \overline{T}\frac{\partial \overline{u_j}}{\partial x_j}\, dV. \tag{7}$$

In this expression, the second term on the r.h.s. should be identically zero in an incompressible fluid due to conservation of mass. However, when this term is measured experimentally, errors in measurement and finite-difference approximations often lead to a non-closure of conservation of mass for an incompressible fluid, which prevents the assumption that the second term on the r.h.s. of Eq. 7 is equal to zero (see Appendix 1). Thus, to obtain an accurate estimation of the total advective flux in the control volume of interest, one should either compute $\int_{CV} \overline{u}_j \frac{\partial \overline{T}}{\partial x_j}\, dV$ or $\int_{CV} \frac{\partial}{\partial x_j}\left(\overline{u_j}\,\overline{T}\right) - \overline{T}\frac{\partial \overline{u}_j}{\partial x_j}\, dV$. Furthermore, we can approximate the second term on the r.h.s. of Eq. 7 as follows

$$\int_{CV} \overline{T}\frac{\partial \overline{u}_j}{\partial x_j}\, dV \approx \overline{T_{\mathcal{V}}} \int_{CV} \frac{\partial \overline{u}_j}{\partial x_j}\, dV = \overline{T_{\mathcal{V}}} \int_{CS} \overline{u}_j \hat{n}_j\, dA, \tag{8}$$

where $T_{\mathcal{V}}$ is a control-volume-averaged temperature. Here, the divergence theorem has been used to transform the volume integral into a surface integral (where the CS subscript indicates a control surface of area A), and $\hat{n}_j$ is the outward-pointing normal vector of each surface of the control volume. As a result, Eq. 6 can now be rewritten as

$$\begin{aligned}\int_{CV} \frac{\partial}{\partial x_j}\left(\overline{u_j T}\right) - \overline{T}\frac{\partial \overline{u}_j}{\partial x_j}\, dV &= \int_{CV} \frac{\partial}{\partial x_j}\left[\overline{u}_j\overline{T} + \overline{u_j' T'}\right] dV - \int_{CV} \overline{T}\frac{\partial \overline{u}_j}{\partial x_j}\, dV \\ &\approx \int_{CS} \left[\overline{u_j}\,\overline{T} + \overline{u_j' T'}\right]\hat{n}_j\, dA - \overline{T_{\mathcal{V}}} \int_{CS} \overline{u_j}\hat{n}_j\, dA \\ &= \int_{CS} \left[\overline{u_j}(\overline{T} - \overline{T}_{\mathcal{V}}) + \overline{u_j' T'}\right]\hat{n}_j\, dA. \end{aligned} \tag{9}$$

Once again, the divergence theorem has been employed, as well as the approximation presented in Eq. 8. It is of relevance to recognize that the correction term corresponds well with the traditional reference temperature introduced in an ad hoc manner to ensure the physical interpretation of the mean or advective flux (Swinbank 1951; Webb et al. 1980; Mauder et al. 2020). This approximation ($\int_{CS}[\overline{u_j}\overline{T_{\mathcal{V}}}]\hat{n}_j dA = \overline{T_{\mathcal{V}}}\int_{CS}\overline{u_j}\hat{n}_j dA$) is further analyzed in Appendix 1.

Next, while the l.h.s. of Eq. 9 provides a measure of the net sensible heat entering the study region, the r.h.s. can be approximated by assuming uniform transport across each face, and transforming the surface integral into a summation,

$$\int_{CS} \left[\overline{u_j}(\overline{T} - \overline{T_{\mathcal{V}}})\right] n_j\, dA = \sum_{CS} \left[\langle \overline{u}_j(\overline{T} - \overline{T_{\mathcal{V}}})\rangle + \langle \overline{u_j' T'}\rangle\right] A\, \hat{n}_j. \tag{10}$$

For the experimental measurements to also be easily interpreted through the perspective of numerical simulations, it is useful at this point to further consider the decomposition of the temporal mean variables into a spatial average and the corresponding spatial fluctuation (Raupach and Shaw 1982). For example, the corresponding temperature field can be decomposed as $\overline{T}(x_j) = \langle \overline{T}\rangle + \overline{T}''$, where the angled brackets denote the spatial average and the double prime indicates a spatial fluctuation from that spatial mean, or dispersive term. Furthermore, the spatial average of the covariance between the mean spatially fluctuating mean

velocity and temperature field is defined as the dispersive flux. By including this dispersive contribution, Eq. 10 can be finally rewritten as

$$\int_{CS} \overline{u_j}(\overline{T} - \overline{T_{\mathcal{V}}})\,\hat{n}_j\,dA = \sum_{CS}\left[\langle\overline{u_j}\rangle\left(\left\langle\overline{T}\right\rangle - \overline{T_{\mathcal{V}}}\right) + \left\langle\overline{u_j}''\overline{T}''\right\rangle + \left\langle\overline{u_j'T'}\right\rangle\right]A\,\hat{n}_j. \tag{11}$$

Here, the terms on the r.h.s. are the bulk advection over the control volume, the dispersive flux, and the volumetric turbulence flux. The dispersive flux quantifies the correlation between spatial fluctuations in the temporal-mean field, where the fluctuations are respectively computed at each surface of the control volume. One of the advantages of this decomposition is that it allows for a direct comparison with the terms in the temperature tendency equation used in standard NWP models (Margairaz et al. 2020b). Specifically, it is straightforward to recognize how the bulk advection term corresponds to the advection term resolved in NWP models. The turbulence flux corresponds to the volumetric subgrid-scale flux, traditionally parametrized with more or less sophisticated methods (Mellor and Yamada 1982). Lastly, the dispersive term is normally neglected or inadvertently disregarded. For this correspondence to be exact, the region of integration should match the grid size in NWP models.

Inspired by the definition of the energy imbalance in Kanda et al. (2004) and Steinfeld et al. (2007) as a means to provide an accurate quantification of the contribution of the bulk advection and dispersive fluxes in the energy transport over a region of interest, we present a modified form of the energy imbalance, which we call the flux imbalance. This extended imbalance accounts for the contribution of both the bulk and dispersive advection, with respect to the well-characterized turbulence flux. This modified imbalance fits more complicated scenarios (i.e., atmospheric stabilities) that are observed in the field, thus providing a more robust understanding of these terms. Specifically, the imbalance I (normalized by the turbulence flux) may be written using the r.h.s. of Eq. 11 as

$$I = \frac{\sum_{CS}\left[\langle\overline{u_j}\rangle\left(\left\langle\overline{T}\right\rangle - \overline{T_{\mathcal{V}}}\right) + \left\langle\overline{u_j}''\overline{T}''\right\rangle + \left\langle\overline{u_j'T'}\right\rangle\right]A\,\hat{n}_j}{\sum_{CS}\left\langle\overline{u_j'T'}\right\rangle A\,\hat{n}_j}, \tag{12}$$

$$= \frac{\sum_{CS}\left[\langle\overline{u_j}\rangle\left(\left\langle\overline{T}\right\rangle - \overline{T_{\mathcal{V}}}\right) + \left\langle\overline{u_j}''\overline{T}''\right\rangle\right]}{\sum_{CS}\left\langle\overline{u_j'T'}\right\rangle A\,\hat{n}_j} + 1. \tag{13}$$

Herein, we use the experimental dataset from the IPAQS heterogeneity project to evaluate all the terms in Eqs. 11 and 12 to determine the potential contribution of spatially dependent, long-lasting (persistent in time) fluctuations on the mean flow. These are thought to be partially responsible for the imbalance of the SEB (Zhou et al. 2018b, 2019; Mauder et al. 2020) and are also usually neglected in NWP models (Margairaz et al. 2020b).

3 Methods

3.1 Experimental Overview

The IPAQS heterogeneity experiment was conducted from 16 June 2019 to 15 July 2019. Field measurements took place at the Surface Layer Turbulence Environmental Science Test (SLTEST) facility at the U.S. Army Dugway Proving Ground, approximately 137 km south-west of Salt Lake City, Utah (40°8'5.9" N, 113°27'7.8" W). The SLTEST facility is characterized by a wide basin stretching $\approx$ 65 km east–west, with a long north–south fetch

($\approx$ 130 km), flat, with a topographical variation of less than 1 m km^{-1}, and a uniform surface roughness of $z_0 = 0.11 \times 10^{-3}$ m (Malek 2003; Hang et al. 2018; Jensen et al. 2016).

The IPAQS heterogeneity field experiment was a large field deployment containing a wide array of sensors. For brevity, only the subset of instrumentation used for the following analysis is described. For further details on the entire experimental layout please refer to Morrison et al. (2020). Figure 1a provides a schematic of a subset of the deployment used here for the analysis, where its defining characteristic is its spatial array of sensors. The distributed set-up was chosen to cover an area equivalent to that of a high-resolution NWP model (i.e. $\sim$1 km^2). To ensure the minimal spatio–temporal error in the deployment, all instruments were surveyed within $\pm$0.5 m spatial accuracy (Leica Total Station, Norcross, Georgia, U.S.), as well as time synchronized to sub 1-ms temporal accuracy through the use of a global positioning system (GPS16-HVS, Garmin, Olathe, Kansas, U.S.). Furthermore, it should be noted that all reported heights are above ground level (a.g.l.).

Seven portable weather instrumentation data systems (PWIDS) (black circles in Fig. 1) were deployed to monitor high-frequency fluctuations of temperature and velocity components over an area of 400 $\times$ 400 m^2, with 200-m spacing. Each station included a three-dimensional sonic anemometer (8100 R. M. Young, Traverse City, Michigan, U.S.) and a fine-wire thermocouple to measure the 2-m temperature and the three components of the turbulent flow at 20 Hz. Two 10-m towers provided vertical-profile measurements across the grid (diamonds in Fig. 1). Each 10-m tower was equipped with three three-dimensional sonic anemometers (CSAT3, Campbell Scientific, Logan, Utah, U.S.) at 2 m, 5 m, and 8 m, orientated at 240°, which was approximately perpendicular to the anticipated mean wind directions ($\approx$330° and 150°) (Jeglum 2016). One of the 10-m towers served also served as the SEB station and included the following additional instrumentation: infrared gas analyzers (IRGA EC150, Campbell Scientific, Logan, Utah, U.S.) at 2 m and 8 m to capture fast response moisture measurements, and three net radiometers (CNR4, Kipp & Zonen, the Netherlands) at 0.5 m, 2 m, and 8 m to measure the four components of the net radiation. Surrounding the 10-m tower there was four 2-m towers equipped with CSAT3 sonic anemometers. The towers to the south and east were also equipped with IRGA EC150s, while the 2-m tower to the west included an array of soil-temperature sensors (depths: 1, 2, 5, 10, 15, 25, 70 cm), and two averaging self-calibrating heat-flux plates (HFP01, Hukseflux, the Netherlands) at a depth of 5 cm and spaced 1.5 m apart.

In addition to the turbulence measurements, four low-cost energy measurement (LEM) stations (purple triangles) were deployed every 200 m, offset by the turbulence masts by 100 m. The LEM stations captured slow-response (0.1 Hz) wind speed, air temperature and humidity at a height of 2 m, and surface temperature, as well as soil temperature at two depths (5 cm, and 20 cm). To capture the spatial distribution of the surface temperature measurements, 13 iButtons (iButtonLink, LLC, Whitewater, Wisconsin, U.S.) were deployed at the surface level next to each station capturing the temperature and humidity every 5 min. Collocation with the surface temperature measurements of the LEM stations ensured accurate measurements of surface temperature for extrapolation to all sites. For the remainder of the work presented herein, we only use the wind speed and temperature measurements from the meteorological towers and iButtons within the red dashed square denoting the perimeter of the top of the control volume in Fig. 1a, b.

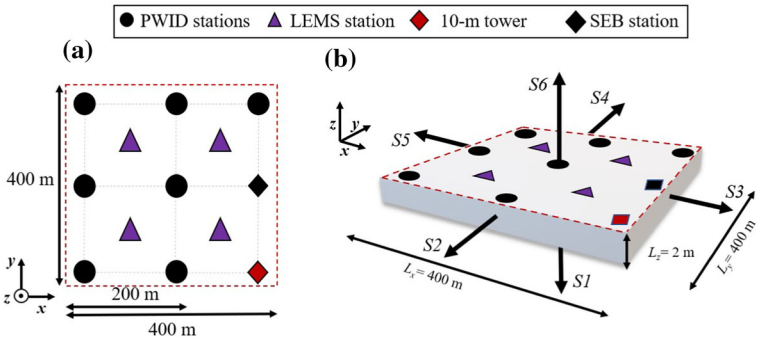

Fig. 1 The **a** experimental layout from the IPAQS19 field experiment used here for this analysis, and **b** a perspective-view schematic of the control volume used for the analysis. Note that the red dashed line in **a** is the above view of the control volume represented in **b**, and the arrows denote the surface normal vector

3.2 Data Treatment

Data were treated with the Utah Turbulence in Environmental Studies Process and Analysis code, developed at The University of Utah (Jensen et al. 2016) from 1–15 July 2019. All data were subject to basic quality control (applying sonic flags and physical limits), as well as a stationarity test (Foken and Wichura 1996). For this analysis, we did not apply a global planar fit to correct for the vertical velocity component due to limited data and poor fits at particular stations. A further discussion of the impact of the vertical velocity component is presented in Appendix 2. A multi-resolution decomposition analysis revealed that all scales of motion tend to be accounted for in 1000 s periods (Vickers and Mahrt 2003); therefore, a linear detrend was applied on the 30-min averaging periods to extract turbulent fluctuations. The data were then rotated into the standard meteorological coordinate system, such that southerly winds correspond to a positive v-velocity component, and westerly winds correspond to a positive u-velocity component. Data were then separated based on completeness, 30-min mean wind speed ($\overline{U}$), and stability ($\zeta = z/L$). Here, z indicates the measurement height above the ground (2 m) and L is the Obukhov length ($L = -\overline{\theta_v} u_*^3 / \kappa g \overline{w'\theta_v'}$), where u_* is the friction velocity, θ_v is the virtual potential temperature, κ is the von Kármán constant ($= 0.4$), g is the acceleration due to gravity ($= 9.8$ m s^{-2}), and $\overline{w'\theta_v'}$ is the vertical kinematic heat flux. Data were isolated as unstable periods ($\zeta \leq -0.1$, with a minimum $\zeta = -142$ observed), stable periods ($\zeta \geq 0.1$, with a maximum $\zeta = 11.9$ observed), free-convective periods ($0 < \overline{U} \leq 4$ m s^{-1}), and forced-convective periods (4 m s^{-1} $< \overline{U} \leq 8$ m s^{-1}). Note that the wind speeds and atmospheric stabilities represent the mean values across the towers used in the control volume analysis at 2 m. This separation was done in order to compare our data with previous LES studies, which only model a range of convective regimes. Moreover, the data segregation used here is consistent with the works of Margairaz et al. (2020a) and Morrison et al. (2020), who showed through LES and experimental studies that unresolved local advection may be stronger on highly convective days due to mean air-temperature differences arising from local surface temperature heterogenities. A summary of the characteristics from the days can be observed in Table 1.

After the data were separated, the terms on the r.h.s. of Eq. 11 (volumetric integral of the total flux over the control volume) were computed. To ensure reliability of the iButton surface-temperature measurements as well as the fine-wire thermocouples, collocation corrections were performed. iButton data were compared with LEM station surface-temperature sensors,

Table 1 The 30-min mean wind speed ($\overline{U}$) and stability ($\zeta = z/L$) for the convective and non-convective days isolated for the analysis

Selected day characteristics				
Period	Free-convective cases		Forced-convective cases	
	$\overline{U}$ (m s^{-1})	ζ	$\overline{U}$ (ms^{-1})	ζ
Day (1000–1600 LT)	2.16	−15.79	5.61	−1.27
Night (0000–0500 LT)	2.31	2.40	5.02	0.90

Note that the times here are in LT (local time = UTC − 6 h)

which were corrected for emissivity (ϵ= 0.95). The sensors' magnitude were found to be similar within an acceptable range with one another (mean R^2 = 0.98 across all stations). Meanwhile, the fine-wire thermocouples were corrected with a second-order polynomial fit with the temperature data from the PB2 station (see Appendix 1 from Morrison et al. 2020 for more details). This tower was chosen due to its proximity to the centre of the control volume and the completeness of its dataset. The 30-min-averaged temperatures were then fit to a logarithmic profile at each station in the analysis. The reference temperature ($T_{\mathcal{V}}$) was calculated from the volumetric average of these values. For the turbulence terms across the vertical faces ($S2$, $S3$, $S4$, and $S5$), a constant-flux layer was assumed in the vertical direction. The profiles from each tower were then used to calculate mean values across the 2-m high faces for the terms in Eq. 11 or in Fig. 1b.

4 Results

Data from the IPAQS heterogeneity campaign were treated based on the methods presented in Sect. 3 and used to compute the total derivative terms [r.h.s. Eq. 11] developed in Sect. 2. Probability density functions (p.d.f.s) of the advection, dispersive, and turbulence terms are built using data from the free- and forced-convective days and presented in Figs. 2 and 3, respectively. Within both figures, the data are further subdivided into unstable ($\zeta \leq -0.1$) and nocturnal periods ($\zeta \geq 0.1$). Note that negative values along the abscissa are indicative of control volume warming rates, while positive values indicate cooling rates. Initial findings show that, for the control volume selected, advection plays a large role in the energy transport and its relative importance (imbalance) may be a function of the mean wind speed.

Here, we use the following standard statistical variables: median ($\tilde{\mu}$), mean (μ_1), standard deviation (μ_2), skewness (μ_3), and kurtosis (μ_4). During daytime periods (Figs. 2a and 3a), the results show that positive turbulence fluxes dominate the budget, with energy going to the surroundings resulting in a decreasing temperature of the control volume on free-convective days (median of $\tilde{\mu}$ = 2.49 K min^{-1}), followed by mean advection and dispersive fluxes. For forced-convective cases, advection of heat from the surroundings into the control volume leads to the largest heating rate ($\tilde{\mu} = -1.99$ K min^{-1}), followed by the turbulence and dispersive fluxes. Broad p.d.f.s describe the observed turbulence fluxes ($\mu_4 = 1.86$ K min^{-1} for free-convective, and $\mu_4 = 2.37$ K min^{-1} for forced-convective periods). However, a more persistent and stronger turbulent flux is observed during free-convective periods ($\tilde{\mu}$ = 2.49 K min^{-1}) when compared to the forced-convective cases, which have a smaller median value ($\tilde{\mu}$ = 1.27 K min^{-1}). Despite this, a larger positive skewness (μ_3 = 0.67 K min^{-1}) during the forced-convective cases is observed, indicating that while on average turbulence fluxes

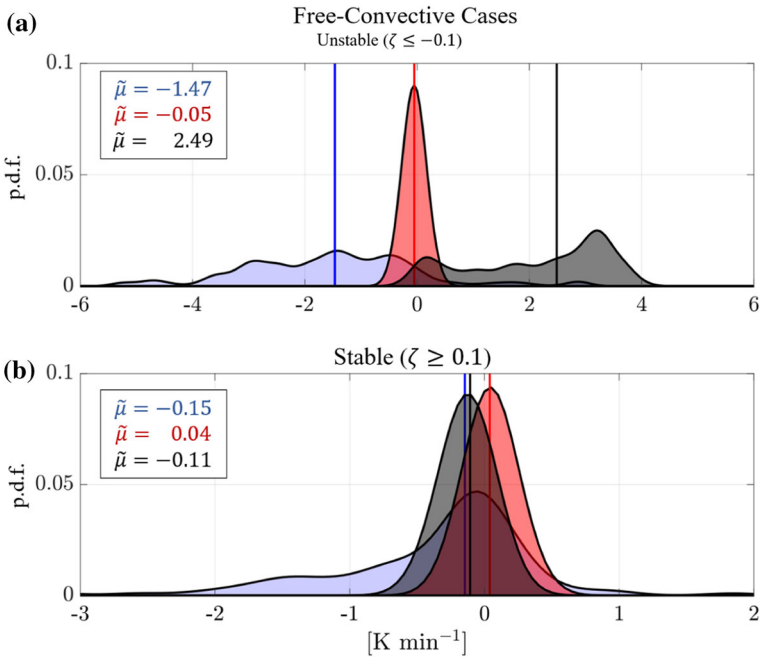

Fig. 2 Normalized p.d.f.s with a kernel fit of the 30-min-averaged bulk advection, dispersive advection, and turbulence terms [from the r.h.s. of Eq. 11] for the free-convective cases in K min^{-1}. The blue, red, and grey shading indicate the bulk advection, the dispersive flux, and the turbulence contributions, respectively. The solid vertical lines represent the median ($\tilde{\mu}$) for each term, whose numeric value is displayed to the left following the colour coding of the p.d.f.s. **a** The unstable free-convective periods, and **b** the calm stable periods from the free-convective days

are less than those observed during free-convective periods, turbulence values of similar, and sometimes greater magnitude, can be observed. This may be the result of intermittency of the turbulence signal during these periods. For the median bulk advection, the values remain primarily negative ($\tilde{\mu} = -1.47$ K min^{-1} for free-convective cases and $\tilde{\mu} = -1.99$ K min^{-1} for forced-convective cases), suggesting that the turbulence and advection modes of transport are working against one another to heat and cool the control volume, respectively. It should be noted that compared to free-convective periods, the forced-convective periods have a larger spread of advective observations ($\mu_2 = 1.55$ K min^{-1} for free-convective cases, and $\mu_2 = 2.94$ K min^{-1} for forced-convective cases). Hence, while the median advection is slightly larger for forced-convective cases, the spread of observed values is much larger. These results are further substantiated through the ratio of the median advection to the median total flux, -47% for free-convective cases and 114% for forced cases. Here, the sign is dominated by the sign of the advection term (negative) to the sign of the total derivative (positive for free-convective periods and negative for forced-convective periods). Lastly, the mean dispersive terms contribute the least to the heat-transport budget compared to advection and turbulence flux with median heating rates of $\tilde{\mu} = -0.05$ K min^{-1} for both the free-convective and forced-convection cases.

During nocturnal periods (Figs. 2b and 3b), the peaks of the p.d.f.s overlap one another, making it difficult at first to discern which transport mode is most relevant. However, in both cases, long negative tails in the advective transport suggest that large intermittent advective

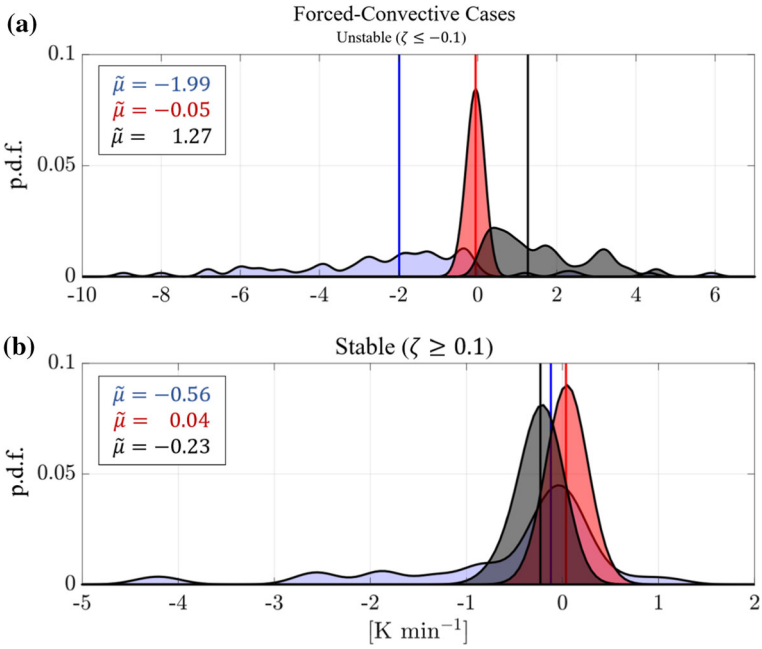

Fig. 3 Normalized p.d.f.s with a kernel fit of the 30-min-averaged bulk and dispersive advection, and the turbulence-flux terms for the forced-convective cases in K min^{-1}. The blue, red, and grey shading indicate the bulk advection, the dispersive advection, and the turbulence-flux contributions, respectfully. Again, the solid vertical lines represent the median ($\tilde{\mu}$) for each term, whose numeric value is displayed to the left following the colour coding of the p.d.f.s. **a** The unstable forced-convective periods, and **b** the stable periods from the forced-convective days

heating of the control volume may occur at night (skewness, $\mu_3 = -1.70$ K min^{-1} for forced-convective periods and $\mu_3 = -1.49$ K min^{-1} for the free-convective cases). Once again, the large negative tail in the advection for the high-wind-speed nocturnal periods produces the largest advection rate observed for this period. While these large periods of heating are not persistent, they appear to be characteristic of high-wind-speed periods. Medians of the terms at night show that for both cases the mean advection is responsible for the majority of the energy transport into the control volume, leading to the largest heating rates. For nocturnal periods on the forced-convective days, advection is responsible for -0.12 K min^{-1} (83% of the total median flux), while during the calmer nocturnal periods this value drops to -0.15 K min^{-1} (86% of the total median flux). Note here the large variance of the advection, which indicates that the advection may heat or cool during nocturnal periods at large rates. This is why, while the median values over the length of the experiment are small, the percent contribution to the total flux on average may be large. Meanwhile, the turbulence flux remains a smaller percent contribution of the total flux during forced and free-convective cases (33% of the total median flux for forced-convective case and 15% of the total median flux). This is likely due to the collapse of turbulence during nocturnal periods and the development of a low-level jet forming from the playa breeze at the SLTEST facility (Fernando et al. 2015). On nights when the playa breeze is absent, calm conditions are observed and turbulent heating of the control volume is almost equally as large in magnitude to the advective heating rates (-0.11 K min^{-1} or 15% of the median total heating). Lastly, the median dispersive contribution

remains fairly equal in magnitude in either case, but countering the advective and turbulent heating through dispersive cooling rates (0.04 K min^{-1} for calm nights or −2% of the median total flux and 0.04 K min^{-1} for high-wind speed nights or −4% of the median total flux). A summary of the main p.d.f. statistics is presented in Table 2.

Given the horizontal scale of the analysis conducted here (400 m), it is important to understand that advective terms may be interpreted as dispersive contributions as the scale of the control volume increases (i.e., NWP grid cell $\mathcal{O}\sim$1 km). To gain a better understanding of this potential dispersive contribution, the imbalance [Eq. 12], or the ratio of the total flux normalized by the turbulence flux is presented in Fig. 4 and rewritten for simplicity as

$$I = \frac{A + D + T}{T} = \frac{A + D}{T} + 1. \tag{14}$$

In Eq. 14, A is the advection term, D is the dispersive term, and T is the turbulence term. Here, an imbalance of less than unity indicates that the sum of advective and dispersive fluxes are of opposite sign to the turbulence. We call this a flux-estimation situation because $A + D + T < T$, and, if one used a single eddy-covariance station, the total flux would be overestimated by a factor of $(A + D)/T$. By normalizing with the turbulence flux, any deviations from a value of unity constitute a flux imbalance. Further, following the same logic, values greater than unity indicate that there is a flux underestimation when compared to turbulence fluxes measured with a single eddy-covariance station.

First, we examine the free-convective daytime case (Fig. 4a), where advection and turbulence fluxes are working to heat and cool the control volume, respectively (as shown in the p.d.f.s in Fig. 2a). In this case, the median imbalance of 0.21 indicates a 79% overestimation of the flux. For the forced-convective daytime case (Fig. 4b), we observe advective transport counteracting the turbulence fluxes, resulting in a median flux imbalance of −0.68 or a 168% overestimation of the flux.

During nocturnal periods, the turbulence flux diminishes and the bulk advective flux becomes the dominate transport term. At the SLTEST facility, during some nocturnal periods, a strong playa breeze from the south can form, leading to strong winds near the surface (Fernando et al. 2015). As a result, we observe large contributions from advection. On nights where this playa breeze is weak or absent, local surface advection and dispersive contributions become relatively important modes of heat transport and can drive a large flux imbalance. In both cases, the median imbalance is greater than unity for nocturnal periods, indicating an underestimation of the flux, and where turbulence and advection are heating the control volume. During forced-convective nights, this underestimation is found to be 43% as a result of the strong playa breeze. While during the free-convective case, we observe the largest median flux imbalance, with a turbulence underestimation of 146%. It should also be noted that due to the collapse of turbulence, the denominator of the imbalance can approach zero leading to large outliers.

To further understand the threshold between the free and forced-convective days and their role in the imbalance, the results are further divided by mean wind speed measured by the 2-m sonic anemometer at the SEB tower (Fig. 5). A box and whisker plot presents the median, and the 25%, and 75% percentiles of the imbalance for wind speed binning, starting at 0 – 1 m s^{-1} and increasing to 6 – 10 m s^{-1}. During the unstable periods, the extrema of the imbalance values reach a local minimum for the 0 – 1 m s^{-1} periods and $I \to 0$ as the wind speeds approach the 3 – 4 m s^{-1} bin. The majority of the box and whisker plots during these periods remains negative, suggesting that only consideration of the turbulence flux would be an overestimation of the flux. The medians and variance appear to increase steadily to a global minimum as higher wind speeds are reached. This result suggests that even during low-wind-

Table 2 Table of statistics for the transport terms from Figs. 2 and 3 (advection, A, dispersive, D, and turbulence, T) and the imbalance, I (Fig. 4)

		Day 1000–1600 LT				Night 0000–0500 LT			
		A	D	T	I	A	D	T	I
Free Convective Cases	$\tilde{\mu}$	−1.47 (−47%)	−0.05 (−1%)	2.49 (145%)	0.21	−0.15 (86%)	0.04 (−2%)	−0.11 (15%)	2.46
	μ_1	−1.53	−0.053	2.15	−0.33	−0.37	0.045	−0.13	6.11
	μ_2	1.55	0.094	1.22	7.90	0.73	0.074	0.091	18.10
	μ_3	0.23	−0.05	−0.47	−5.92	−1.01	0.59	−0.64	1.39
	μ_4	3.61	2.68	1.86	75.23	5.49	3.96	2.98	11.93
Forced Convective Cases	$\tilde{\mu}$	−1.99 (114%)	−0.05 (1%)	1.27 (−21%)	−0.68	−0.12 (83%)	0.04 (−4%)	−0.23 (33%)	1.43
	μ_1	−2.38	−0.07	1.60	−1.74	−0.56	0.05	−0.24	6.52
	μ_2	2.94	0.13	1.23	9.40	1.13	0.10	0.16	15.22
	μ_3	−0.19	−0.79	0.67	−1.40	−1.70	0.17	−1.10	3.41
	μ_4	4.13	3.49	2.37	14.02	5.72	4.50	4.06	14.21

For each case, $\tilde{\mu}$ is the median, μ_1 the mean, μ_2 the standard deviation, μ_3 the skewness, and μ_4 the kurtosis. The advection, dispersive, and turbulence-flux terms are presented in K min^{-1}, while the imbalance is dimensionless. Additionally, the median ratio of the terms to the total heat flux [r.h.s. of Eq. 11] are provided in parentheses

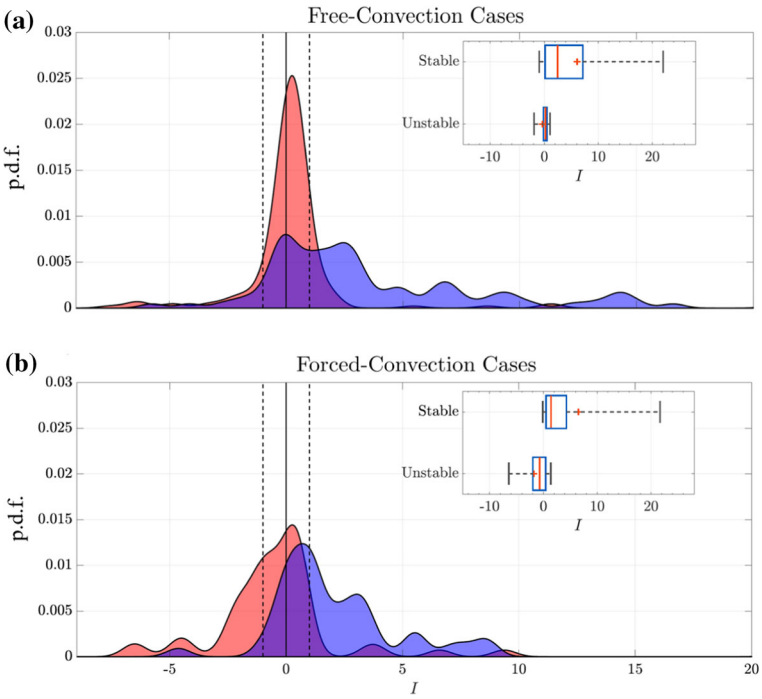

Fig. 4 Normalized p.d.f.s with a kernel fit for the flux imbalance for all cases. Here red shading denotes the daytime periods, while blue the nocturnal. The vertical black solid line denotes zero, while the black dashed lines denote −1 and 1. Insets in the figures present the box and whisker plot for each case to present outlying data, which are prevalent in the nocturnal case when turbulence approaches zero. **a** The free-convective cases and the respective calm nocturnal periods and **b** the forced-convective periods and their respective high-wind speed nocturnal periods

speed cases, the relative strength of the advection and dispersive fluxes driven by mean flow perturbations can be as large as during the high-wind-speed counter periods. Meanwhile, during stable periods, the largest imbalances and range of imbalances are observed in the $0 - 1$ m s^{-1} and the $1 - 2$ m s^{-1} bins. Similar to the behaviour observed in the unstable cases, the imbalance decreases to a local minimum for the $3 - 4$ m s^{-1} cases and steadily increases for higher wind speeds. This result demonstrates the importance of advection and dispersive fluxes at low wind speeds ($0 - 1$ m s^{-1}) for both stable and unstable cases, whose relative importance appears to steadily decrease until the $3 - 4$ m s^{-1} regime for unstable cases and the $4 - 5$ m s^{-1} regime for stable cases, then increase for higher wind speed cases. This result may reflect mean temperature field structural differences, such as convective cell-type structures during low wind speed unstable cases, transforming to elongated roll type structures for higher wind speed cases.

5 Discussion

Results presented herein show a large flux imbalance occurring over a near-conical desert playa with significant surface thermal heterogenities. Four characteristic classes are examined, each demonstrating the importance of spatially distributed measurements for accurate

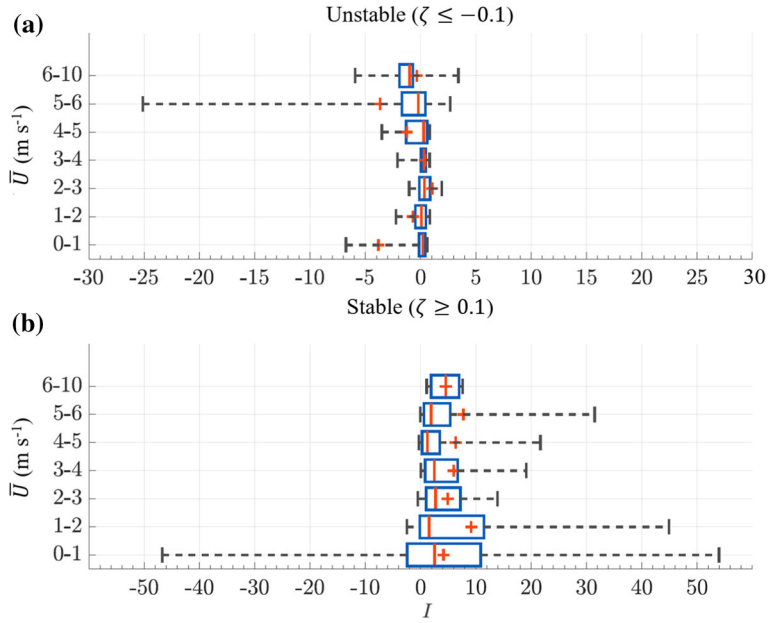

Fig. 5 A box and whisker plot of the flux imbalance binned by mean wind speed for **a** unstable periods ($\zeta \leq -0.1$) and **b** stable periods ($\zeta \geq 0.1$). The l.h.s. of the box represents the 25% percentile and the r.h.s. of the box is the 75% percentile, respectively. Meanwhile, the vertical red line inside the box is the median, the and the error bars indicate the extent of the most extreme data points not considered outliers

assessment of advective and dispersive fluxes. In agreement with previous literature, which solely focuses on the flux imbalance for the vertical component of transport for convective periods, we find large flux imbalances under convective regimes. In particular, during strong daytime free-convective periods, we observe a flux overestimation of 79%, meanwhile during the forced-convective regime we observe a flux overestimation of 168%. This large flux imbalance observed on free-convective days is likely caused by quasi-stationary secondary circulations driven by the surface thermal heterogeneities inducing persistent mean air temperature gradients. These mean air-temperature gradients, which promote advection, work with turbulence fluxes to increase heat transport into the control volume. This differs from the forced-convective periods, where strong advective transport is likely shear dominated from larger-scale forcing, which act with turbulence heating to heat the control volume.

During stable periods, we find an increasingly important flux imbalance with the collapse of turbulence and strong winds. For those periods, traditional single-tower flux measurements underestimate the total energy flux by 43% on average, while for quiescent nights this value increases to 146%. The physical explanation behind the nocturnal-period imbalance can be understood by investigating the dominate transport terms in each case. During strong-wind nights, we observe a complete collapse of turbulence and very weak dispersive contributions. The dominant advective force is most likely arising from a strong southerly playa breeze, which is driven through the large thermal gradients between the Great Salt Lake to the north and the warmer surrounding areas to the south. Surrounding terrain features provide a convergence of wind through the SLTEST site, strengthening this playa breeze. With this larger scale thermal gradient, complementary terrain, and small surface roughness across the desert basin, low-level jets can form and lead to large values of the advection term, such as the

ones observed here. In comparison, on quiescent evenings, surface thermal perturbations can penetrate the air aloft more effectively, and by comparison to turbulence, advective transport is relatively more important. Interestingly, we observe that the dispersive contribution is working to cool the control volume, while advection and turbulence fluxes are working to heat it. This may be partially a result of the precise location of our control volume, since the impact of the surface thermal effects are highly localized during weak-wind nocturnal periods. During stable periods, while the median turbulence-flux term can be of the order of the advection term, the median percent contribution is much less. This is due in part to that intermittency of the turbulence and the large negative values which can be observed from the advection. We suggest that future work should include an expanded analysis covering different control volumes, which could provide further insight into the reason behind these competing forms of heat transport over a seemly flat surface.

The large bias of single-tower measurements has implications for the SEB closure, even for data collected over this seemingly ideal location. Within the SEB community, persistent flow heterogeneities have often been identified as culprits for the SEB residual (Mauder et al. 2020). These flow perturbations, which appear to be more relevant during low-wind-speed periods (Margairaz et al. 2020a), could be resolved as advection or dispersive fluxes depending on the scales of the observations. From the presented results it is clear that a three-dimensional SEB is required to capture these transport terms. Moreover, results may become more robust by improving accuracy and measurement resolution, with emphasis on the latter. Results presented here are computed with a control volume of the scales of $400 \times 400 \times 2$ m^3 with towers spaced evenly every 200 m over the control volume. Future field experiments, particularly those utilizing optical fibre air-temperature measurements, may provide the next step in understanding and measuring the three-dimensional surface energy balance at scales of $\mathcal{O}\ 1-100$ m (Thomas et al. 2011; Zeeman et al. 2014). However, in order to fully complement these forthcoming approaches to the scales of NWP models, spatially distributed sensors over a larger experimental domain may be required. Experiments such as the Chequamegon Heterogeneous Ecosystem Energy-balance Study Enabled by a High-density Extensive Array of Detectors (CHEESEHEAD) (Butterworth et al. 2020, 2021), which captured data over $\mathcal{O}$ 10 km scales with a large array of towers over a forested canopy, may be the step forward in understanding this issue at larger scales. Lastly, expansion of similar three-dimensional analysis over a variety of surfaces may shed light on energy-balance residuals over vegetated surfaces or within vegetated canopies, where energy storage and moisture fluxes may be more relevant (Oncley et al. 2007).

The large flux imbalance is also important in the context of NWP models. Here, the experimental control-volume domain size used in this analysis and how it relates to the inherent space filtering arising in NWP models is an important consideration for sub-grid scale modelling. Currently, NWP simulations model the turbulence flux over individual grid cells at scales of $\mathcal{O}$ 1 km with a variety of methods to estimate the impact of surface heterogeneities on the flow (Bou-Zeid et al. 2020). Based on the spatial decomposition scheme from Raupach and Shaw (1982), the scales at which the spatial averaging is computed are inherently defining the scale at which we capture dispersive or advective fluxes. These long-lasting flow perturbations leading to advective and dispersive fluxes are neither resolved by the bulk advection in the model or through classical turbulence closure schemes, which assume isotropic turbulence (Stoll et al. 2020). In order to capture the unresolved advection in numerical models, the models must aim to parametrize the dispersive advection term. This is extremely important in the context of mesoscale weather forecasting tools, such as the WRF model, which solves for the bulk advection term on the order of 1–5 km and models the turbulent heat exchange over that grid cell. From numerical experiments, it has been shown that several variables

(i.e., friction velocity and surface temperature heterogeneity strength) may be relevant when understanding the impact of the surface heterogeneity and the flux imbalance, requiring further experimental validation of these approaches (De Roo and Mauder 2018, Margairaz et al. 2020a, Margairaz et al. 2020b). Between the demonstrated large flux imbalance observed here and the promising numerical studies driving our understanding behind surface heterogeneity, it is import that future experimental studies increasingly examine these processes as a function of variable surface forcings.

6 Conclusions

Herein, a control volume analysis of the substantial derivative of the temperature tendency equation at scales $\mathcal{O}$ 100 m over the SLTEST facility was performed with the IPAQS heterogeneity campaign dataset. The analysis was divided amongst four stability cases. Results demonstrate the importance of capturing locally driven mean advective and dispersive contributions in relation to the turbulent flux through quantification of the flux imbalance [Eq. 12]. For unstable free-convective periods, a median imbalance of 79% (flux overestimation) was observed, while for forced-convective periods the median imbalance rose to 168% (flux overestimation). Further analysis shows that the imbalance may be a function of wind speed and provides evidence that during strongly convection periods, persistent air-temperature differences may be as prevalent in the surface layer compared to the mean air-temperature differences observed during shear driven stabilities. Meanwhile, during high-wind-speed nocturnal periods, a median imbalance of 43% was observed, which rose to 146% for quiescent nights. By contrast to the daytime convective periods, nocturnal periods with the weakest winds produced the largest imbalance. This imbalance was primarily driven by persistent air-temperature differences driving strong local advection. Meanwhile during strong forced-convective nocturnal periods, the imbalance was most likely attributed to the development of a low-level jet related to a playa breeze.

These large observed imbalances also provide evidence to support a future study of the three-dimensional SEB. Due to the mean advective and dispersive fluxes' relevance, it may be important under certain conditions for the SEB closure, and future SEB experiments should consider measuring, at minimum, the horizontal advection, even over seemly homogeneous terrain. Lastly, it is important to note the relevance of this imbalance analysis in the context of numerical simulations, which utilize the Reynolds-averaged Navier–Stokes equations for mesoscale weather forecasting. The bulk advective and dispersive fluxes computed at scales of $\mathcal{O}$ 100 m are otherwise absent terms in subgrid-scale models and present critical observations that should be considered in future developments of these models. In order to continue this work and to improve NWP model accuracy, further experimental studies with high-resolution data at multiple scales are required for a parametrization of these terms.

Acknowledgements This project has been conducted with the support of a U.S. National Science Foundation (Grant No. PDM-1649067). Marc Calaf thanks the support of the National Science Foundation Grants PDM-1649067, and PDM-1712538 as well as the support of the Alexander von Humboldt Stiftung/Foundation, *Humboldt Research Fellowship for Experienced Researchers*, during the sabbatical year at the Karlsruhe Institute of Technology Campus Alpin in Garmisch-Partenkrichen. The authors are also thankful Dr. Dragan Zajic and the U.S. Army Dugway Proving Ground for their gracious assistance and for providing the experimental test bed. The authors declare no conflict of interest.

Appendix 1: Validation of the Temperature Reference

Throughout boundary-layer literature, experimental estimates of heat or moisture advection often include a scalar reference term to maintain representative measurements. However, the scalar reference term is often loosely defined and changes based on the user's perspective (Swinbank 1951; Webb et al. 1980; Mauder et al. 2020). Moreover, the reference term is generally added in an ad hoc fashion without mathematical support. In Eq. 9, a mathematical derivation of the scalar reference correction is presented for temperature. The derivation assumes that the product of the temperature and the divergence of the velocity field can be separated to apply the divergence theorem. With this assumption, it is then possible to rewrite the advection component of the flux as $\overline{u}_j\overline{T} - \overline{u}_j\overline{T}_{\mathcal{V}}$. Which states that estimated scalar advection is corrected for by the volumetric average of the scalar by the velocity field, or in other words, the scalar advection is corrected for the inability to properly conserve mass with coarse field measurements. This explanation is the likely reason why the strong form of the scalar advection ($\partial_{x_j}\overline{u}_j\overline{T}$) is absent from the experimental atmospheric boundary-layer literature.

To validate the use of the scalar reference value when computing advection, data from IPAQS were used to evaluate the following balance

$$\int_{CV} \overline{u}_j \frac{d\overline{T}}{dx_j} dV = \int_{CS} [\overline{u}_j\overline{T}_{\mathcal{V}}]\hat{n}_j dA - \overline{T}_{\mathcal{V}} \int_{CS} \overline{u}_j \hat{n}_j dA. \tag{15}$$

Specifically, we compare the computed total advection minus the correction term with the weak form of the volume integral of the flux. The same control volume described in the analysis is also used here ($400 \times 400 \times 2$ m^3). In order to obtain these terms, several assumptions were made to handle the coarse grid over the control volume. As described in the main document of the paper, the horizontal velocities and temperatures were fit with a logarithmic profile. Due to the coarseness of the grid, the integrand was assumed constant across the face of the surface with a value of the spatial average. Additionally, due to lack of understanding of the vertical functional form of w near the surface, a linear fit with a no-slip condition was applied.

The terms in Eq. 15 were computed for 11 days using 30-min averages and are presented in Fig. 6. The median relative difference between the l.h.s. and r.h.s. of Eq. 15 over the 11 days analyzed was 19%, with the largest observed errors occurring during from 4 July 2019 to 6 July 2019, during a power outage which removed two towers from the control volume. During the power outage, the median relative error was 94%, while removal of this

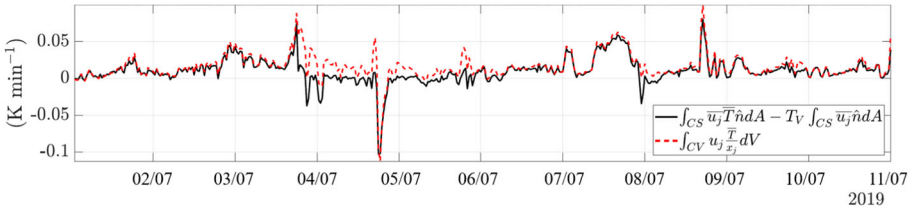

Fig. 6 Validation of the scalar reference value for experimental computation of the advection term. Data were averaged every 30 min over 11 days. The black solid line presents the volume integral of the strong form of the advection with the scalar reference term subtracted, while the red dashed line presents the volume integral of the weak form of the flux. Note the increase in relative error between the methods from the evening on 3 July 2019 to 6 July 2019 arising from a power outage leading to a decrease in tower density

period reduces the median relative error to 14%. A sensitivity analysis designed to determine the number of towers needed to fully capture the complete advection indicates that as the number of towers inside the control volume decreases, the relative error increases. Moreover, the relative error is also a function of the location of the towers removed, indicating a spatial sensitivity to tower placement as well number of towers. This result indicates that the number of towers necessary to capture the entire flux is likely a function of the surface conditions (heterogeneity), density of towers, and control volume size and requires further study to parametrize the required number of towers to properly capture the complete flux from the surface. Furthermore, while this analysis is a first with regard to the scalar reference values used to compute the experimental advection, further insight from numerical studies would provide valuable information in understanding the impact of the reference temperature.

Appendix 2: Global Planar Fit with an Array of High-Density Towers

Due to the aspect ratio and limited complete dataset, caution was taken when treating the variables needed for the analysis. Of particular interest was the vertical velocity component w, since the area of the top of the control volume was 50 times larger than the sum of the horizontal faces. Most often, a global planar fit over the available data is performed (Wilczak et al. 2001) to correct for any biases in the deployment of the instruments. Figure 7 presents the kernel-fit p.d.f.s of both the raw and global planar fit vertical velocity components. While the statistics for some stations appear to remain similar (i.e., PA3), in some cases the spread of the p.d.f.s widen significantly, contaminating the signal (i.e., PC4).

The relative error of the global planar fit was tested further as a function of wind angle, however the amount of available data was at the threshold of the 15-day minimum for a reliable fit to be applied. Despite this, since our stations were deployed over an idealized surface with extreme care, for the analysis the raw vertical velocity signal provided a fair compromise. In more complex experiments with an array of flux towers, this analysis begs the question if the local global planar fit is the correct methodology for planar array experiments. While many experiments have studied the observed velocities between a variety of sonics

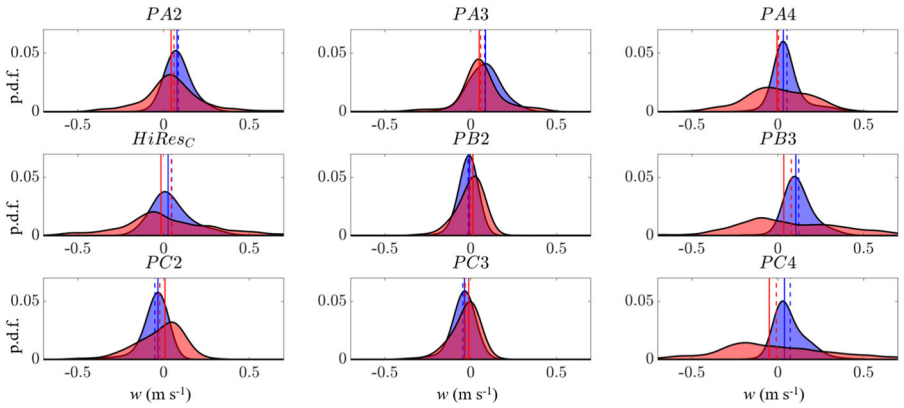

Fig. 7 Kernel fit p.d.f.s of the raw measured vertical velocity component (blue) and the global planar fit (red). Each subplot represents the station used in the control volume analysis. The vertical solid line represents the median, while the dashed line represents the mean

(Mauder and Zeeman 2018) and relative errors (Horst et al. 2015) further studies into the treatment of coordinate system should take place. For example, studies examining the impact of no global planar fit, a local global planar fit (time, $\overline{w} = 0$), and a two-dimensional global planar fit (space-time, $\langle \overline{w} \rangle = 0$) would be insightful as horizontal-array experiments become common place.

References

Bou-Zeid E, Anderson W, Katul G, Marht L (2020) The persistent challenge of surface heterogeneity in boundary-layer meteorology: a review. Boundary-Layer Meteorol. https://doi.org/10.1007/s10546-020-00551-8

Butterworth BJ, Desai AR, Metzger S, Townsend PA, Schwartz MD, Petty GW, Mauder M, Vogelmann H, Andresen CG, Augustine TJ et al (2020) Connecting land-atmosphere interactions to surface heterogeneity in CHEESEHEAD 2019. Earth Space Sci Open Arch. https://doi.org/10.1002/essoar.10503532.1

Butterworth BJ, Desai AR, Metzger S, Townsend PA, Schwartz MD, Petty GW, Mauder M, Vogelmann H, Andresen CG, Augustine TJ, Bertram TH, Brown WOJ, Buban M, Cleary P, Durden DJ, Florian CR, Iglinski TJ, Kruger EL, Lantz K, Lee TR, Meyers TP, Mineau JK, Olson ER, Oncley SP, Paleri S, Pertzborn RA, Pettersen C, Plummer DM, Riihimaki LD, Guzman ER, Sedlar J, Smith EN, Speidel J, Stoy PC, Sühring M, Thom JE, Turner DD, Vermeuel MP, Wagner TJ, Wang Z, Wanner L, White LD, Wilczak JM, Wright DB, Zheng T (2021) Connecting land-atmosphere interactions to surface heterogeneity in CHEESEHEAD19. Bull Am Meteorol Soc 102(2):E421–E445. https://doi.org/10.1175/BAMS-D-19-0346.1

Culf AD, Foken T, Gash JHC (2004) The energy balance closure problem, pp 159–166. Springer, Berlin Heidelberg https://doi.org/10.1007/978-3-642-18948-713

De Roo F, Mauder M (2018) The influence of idealized surface heterogeneity on virtual turbulent flux measurements. Atmos Chem Phys 18(7):5059–5074. https://doi.org/10.5194/acp-18-5059-2018

Desai A, Xu K, Suhring M, Metzger S, Durden D, Petty GW, Townsend PA, Thom JE, Schwartz MD, Mauder M (2018) The infinite flux tower project: Contribution of land surface energy-balance heterogeneity to mesoscale circulations and flux tower biases. American Geophysical Union Fall Meeting

Fernando HJS, Pardyjak ER, Di Sabatino S, Chow FK, De Wekker SFJ, Hoch SW, Hacker J, Pace JC, Pratt T, Pu Z, Steenburgh WJ, Whiteman CD, Wang Y, Zajic D, Balsley B, Dimitrova R, Emmitt GD, Higgins CW, Hunt JCR, Knievel JC, Lawrence D, Liu Y, Nadeau DF, Kit E, Blomquist BW, Conry P, Coppersmith RS, Creegan E, Felton M, Grachev A, Gunawardena N, Hang C, Hocut CM, Huynh G, Jeglum ME, Jensen D, Kulandaivelu V, Lehner M, Leo LS, Liberzon D, Massey JD, McEnerney K, Pal S, Price T, Sghiatti M, Silver Z, Thompson M, Zhang H, Zsedrovits T (2015) The MATERHORN: unraveling the intricacies of mountain weather. Bull Am Meteorol Soc 96(11):1945–1967. https://doi.org/10.1175/BAMS-D-13-00131.1

Finnigan JJ, Clement R, Malhi Y, Leuning R, Cleugh H (2003) A re-evaluation of long-term flux measurement techniques part i: averaging and coordinate rotation. Boundary-Layer Meteorol 107(1):1–48. https://doi.org/10.1023/A:1021554900225

Foken T (2008) The energy balance closure problem: an overview. Ecol Appl 18(6):1351–1367. https://doi.org/10.1890/06-0922.1

Foken T, Wichura B (1996) Tools for quality assessment of surface-based flux measurements. Agric For Meteorol 78(1):83–105. https://doi.org/10.1016/0168-1923(95)02248-1

Garcia-Santos V, Cuxart J, Jimenez MA, Martinez-Villagrasa D, Simo G, Picos R, Caselles V (2019) Study of temperature heterogeneities at sub-kilometric scales and influence on surface-atmosphere energy interactions. IEEE Trans Geosci Remote 57(2):640–654. https://doi.org/10.1109/TGRS.2018.2859182

Hang C, Jensen D, Hoch S, Paryjak ER (2018) Playa soil moisture and evaporation dynamics during the materhorn field program. Boundary-Layer Meteorol 3:521–538. https://doi.org/10.1007/s10546-015-0058-0

Higgins CW (2012) A-posteriori analysis of surface energy budget closure to determine missed energy pathways. Geophys Res Lett. https://doi.org/10.1029/2012GL052918

Horst T, Semmer S, Maclean G (2015) Correction of a non-orthogonal, three-component sonic anemometer for flow distortion by transducer shadowing. Boundary-Layer Meteorol 155:371–395. https://doi.org/10.1007/s10546-015-0010-3

Jeglum ME (2016) Multiscale flow interactions in the complex terrain of northwestern utah. PhD thesis, University of Utah

Jensen DD, Nadeau DF, Hoch SW, Pardyjak ER (2016) Observations of near-surface heat-flux and temperature profiles through the early evening transition over contrasting surfaces. Boundary-Layer Meteorol 159:567–587

Kanda M, Inagaki A, Letzel MO, Raasch S, Watanabe T (2004) LES study of the energy imbalance problem with eddy covariance fluxes. Boundary-Layer Meteorol 110(3):381–404. https://doi.org/10.1023/B:BOUN.0000007225.45548.7a

Kukharets V, Tsvang L (1999) Variations in the underlying surface temperature and the problem of closure of the heat balance equation. Izv Atmos Ocean Phys 35:188–194

Kukharets VP, Nalbandyan HG, Foken T (2000) Thermal interactions between the underlying surface and a nonstationary radiation flux. Izv Atmos Ocean Phys 36(3):318–325

Malek E (2003) Microclimate of a desert playa: evaluation of annual radiation, energy, and water budgets components. Int J Climatol 23:333–345

Margairaz F, Pardyjak E, Calaf M (2020a) Effect of the land surface thermal patchiness on the atmospheric boundary layer through a quantification of the dispersive fluxes. Boundary-Layer Meteorol

Margairaz F, Pardyjak E, Calaf M (2020) Surface thermal heterogeneities and the atmospheric boundary layer: the thermal heterogeneity parameter. Boundary-Layer Meteorol 177:49–68. https://doi.org/10.1007/s10546-020-00544-7

Mason P (1995) Atmospheric boundary layer flows: their structure and measurement. Boundary-Layer Meteorol 62(72):213–214. https://doi.org/10.1007/BF00712396

Mauder M, Zeeman MJ (2018) Field intercomparison of prevailing sonic anemometers. Atmos Meas Tech 11(1):249–263. https://doi.org/10.5194/amt-11-249-2018

Mauder M, Foken T, Cuxart J (2020) Surface energy balance closure over land: A review. Boundary-Layer Meteorol 177:395–426. https://doi.org/10.1007/s10546-020-00529-6

Mellor GL, Yamada T (1982) Development of a turbulence closure model for geophysical fluid problems. Rev Geophys 20(4):851–875

Morrison T, Calaf M, Higgins CW, Drake SA, Perelet A, Pardyjak E (2020) The impact of surface temperature heterogeneity on near-surface heat transport. Boundary-Layer Meteorol. https://doi.org/10.1007/s10546-021-00624-2

Oncley SP, Foken T, Vogt R, Kohsiek W, DeBruin HA, Bernhofer C, Christen A, van Gorsel E, Grantz D, Feigenwinter C, Lehner I, Liebethal C, Liu H, Mauder M, Pitacco A, Ribeiro L, Weidinger T (2007) The energy balance experiment EBEX-2000. Part i: overview and energy balance. Boundary-Layer Meteorol 123(1):1–28. https://doi.org/10.1007/s10546-007-9161-1

Pardyjak E, Calaf M, Hultmark M, Higgins CW, Iungo G, Zajic D, Perelet AO, Morrison T, Gunawardena N, Brunner C, Huang YC, Drake SA, DeBell T, Schwartz C, Najafi B, Puccioni M, Hoch S, Letizia S, Kokmanian K (2018) An overview of the idealized planar array experiment for quantifying surface heterogeneity (IPAQS) in the atmospheric surface layer experiment (invited). American Geophysical Union Fall Meeting

Paw U, Baldocchi DD, Meyers T, Wilson K (2000) Correction of eddy-covariance measurements incorporating both advective effects and density fluxes. Boundary-Layer Meteorol pp 487–511

Peters-Lidard CD, Blackburn E, Liang X, Wood EF (1998) The effect of soil thermal conductivity parameterization on surface energy fluxes and temperatures. J Atmos Sci 55(7):1209–1224. https://doi.org/10.1175/1520-0469(1998)055<1209:TEOSTC>2.0.CO;2

Raupach MR, Shaw RH (1982) Averaging procedures for flow within vegetation canopies. Boundary-Layer Meteorol 22(1):79–90. https://doi.org/10.1007/BF00128057

Steinfeld G, Letzel MO, Raasch S, Kanda M, Inagaki A (2007) Spatial representativeness of single tower measurements and the imbalance problem with eddy-covariance fluxes: results of a large-eddy simulation study. Boundary-Layer Meteorol 123(1):77–98. https://doi.org/10.1007/s10546-006-9133-x

Stoll R, Gibbs J, Salesky S, Anderson W, Calaf M (2020) Large-eddy simulation of the atmospheric boundary layer. Boundary-Layer Meteorol. https://doi.org/10.1007/s10546-020-00556-3

Swinbank WC (1951) The measurement of vertical transfer of heat and water vapor by eddies in the lower atmosphere. J Meteorol 8(3):135–145. https://doi.org/10.1175/1520-0469(1951)008<0135:TMOVTO>2.0.CO;2

Thomas CK, Kennedy AM, Selker JS, Moretti A, Schroth MH, Smoot AR, Tufillaro NB, Zeeman MJ (2011) High-resolution fibre-optic temperature sensing: a new tool to study the two-dimensional structure of atmospheric surface-layer flow. Boundary-Layer Meteorol 142:177–192

Vickers D, Mahrt L (2003) The cospectral gap and turbulent flux calculations. tmos and Oceanic Technol 20(5):660–672, https://doi.org/10.1175/1520-0426(2003)20<660:TCGATF>2.0.CO;2

Webb EK, Pearman GI, Leuning R (1980) Correction of flux measurements for density effects due to heat and water vapour transfer. Q J Roy Meteorol Soc 106(447):85–100. https://doi.org/10.1002/qj.49710644707
Wilczak JM, Oncley SP, Stage SA (2001) Sonic anemometer tilt correction algorithms. Boundary-Layer Meteorol 99(1):127–150. https://doi.org/10.1023/A:1018966204465
Zeeman MJ, Selker JS, Thomas CK (2014) Near-surface motion in the nocturnal, stable boundary layer observed with fibre-optic distributed temperature sensing. Boundary-Layer Meteorol 154:189–205
Zhou Y, Li D, Liu H, Li X (2018) Diurnal variations of the flux imbalance over homogeneous and heterogeneous landscapes. Boundary-Layer Meteorol 168(3):417–442. https://doi.org/10.1007/s10546-018-0358-2
Zhou Y, Li D, Liu H, Li X (2018) Diurnal variations of the flux imbalance over homogeneous and heterogeneous landscapes. Boundary-Layer Meteorol 168:417–442. https://doi.org/10.1007/s10546-018-0358-2
Zhou Y, Li D, Li X (2019) The effects of surface heterogeneity scale on the flux imbalance under free convection. J Geophys Res Atmos. https://doi.org/10.1029/2018JD029550